

Experimental investigation of wave tip variability of impacting waves

van Meerkerk, M.; Poelma, C.; Hofland, B.; Westerweel, J.

DOI

[10.1063/5.0016467](https://doi.org/10.1063/5.0016467)

Publication date

2020

Document Version

Final published version

Published in

Physics of Fluids

Citation (APA)

van Meerkerk, M., Poelma, C., Hofland, B., & Westerweel, J. (2020). Experimental investigation of wave tip variability of impacting waves. *Physics of Fluids*, 32(8), Article 082110. <https://doi.org/10.1063/5.0016467>

Important note

To cite this publication, please use the final published version (if applicable).
Please check the document version above.

Copyright

Other than for strictly personal use, it is not permitted to download, forward or distribute the text or part of it, without the consent of the author(s) and/or copyright holder(s), unless the work is under an open content license such as Creative Commons.

Takedown policy

Please contact us and provide details if you believe this document breaches copyrights.
We will remove access to the work immediately and investigate your claim.

Green Open Access added to TU Delft Institutional Repository

'You share, we take care!' - Taverne project

<https://www.openaccess.nl/en/you-share-we-take-care>

Otherwise as indicated in the copyright section: the publisher is the copyright holder of this work and the author uses the Dutch legislation to make this work public.

Experimental investigation of wave tip variability of impacting waves ^{EP}

Cite as: Phys. Fluids **32**, 082110 (2020); <https://doi.org/10.1063/5.0016467>

Submitted: 05 June 2020 . Accepted: 03 August 2020 . Published Online: 20 August 2020

 M. van Meerkerk,  C. Poelma,  B. Hofland, and  J. Westerweel

COLLECTIONS

 This paper was selected as an Editor's Pick



View Online



Export Citation



CrossMark

ARTICLES YOU MAY BE INTERESTED IN

[Investigation of cavitation and vapor shedding mechanisms in a Venturi nozzle](#)

Physics of Fluids **32**, 083306 (2020); <https://doi.org/10.1063/5.0015487>

[Low Reynolds number turbulent flows over elastic walls](#)

Physics of Fluids **32**, 083109 (2020); <https://doi.org/10.1063/5.0018770>

[On coherent structures of spatially oscillating planar liquid jet developing in a quiescent atmosphere](#)

Physics of Fluids **32**, 082111 (2020); <https://doi.org/10.1063/5.0016480>

Physics of Fluids

SPECIAL TOPIC: Tribute to
Frank M. White on his 88th Anniversary

SUBMIT TODAY!



Experimental investigation of wave tip variability of impacting waves

Cite as: Phys. Fluids 32, 082110 (2020); doi: 10.1063/5.0016467

Submitted: 5 June 2020 • Accepted: 3 August 2020 •

Published Online: 20 August 2020



M. van Meerkerk,¹  C. Poelma,^{1,a)}  B. Hofland,²  and J. Westerweel³ 

AFFILIATIONS

¹3ME, Process and Energy, Multiphase Systems, Delft University of Technology, Leeghwaterstraat 39, 2628 CB Delft, The Netherlands

²CEG, Hydraulic Engineering, Delft University of Technology, Stevinweg 1, 2628 CN Delft, The Netherlands

³3ME, Process and Energy, Fluid Mechanics, Delft University of Technology, Leeghwaterstraat 39, 2628 CB Delft, The Netherlands

^{a)} Author to whom correspondence should be addressed: C.Poelma@tudelft.nl

ABSTRACT

We present an experimental study on the variation in wave impact location and present a mechanism for the development of free surface instabilities on the wave crest for repeatable plunging wave impacts on a vertical wall. The existence of free surface instabilities on an impacting wave is well known, but their characteristics and formation mechanism are relatively unknown. The development of the global wave shape is measured using a visualization camera, whereas the local wave shape is measured with an accurate stereo-planar laser-induced fluorescence technique. A repeatable wave is generated with negligible system variability. The global wave behavior resembles that of a plunging breaker, with a gas pocket cross-sectional area defined by an ellipse of constant aspect ratio. The variability of the local wave profile increases significantly as it approaches the wall. The impact location varies by $\sim 0.5\%$ of the wave height or more than a typical pressure sensor diameter. Additionally, the wave tip accelerates to a velocity of $1.5\sqrt{gh_0}$ compared to the global wave velocity of $1.2\sqrt{gh_0}$. The difference in impact location and velocity can result in a pressure variation of $\sim 25\%$. A mechanism for instability development is observed as the wave tip becomes thinner and elongates when it approaches the wall. A flapping liquid sheet develops that accelerates the wave tip locally and this triggers a spanwise Rayleigh–Taylor instability.

Published under license by AIP Publishing. <https://doi.org/10.1063/5.0016467>

I. INTRODUCTION

In recent years, the liquefied natural gas (LNG) market showed significant growth with an increased demand for floating liquefaction facilities, storage facilities, and shipping solutions. Furthermore, LNG is proposed as an alternative shipping fuel, especially with the prospect of stricter emission standards.¹ New challenges arise with the widespread use of LNG, such as the growth in bulk capacity of containment systems, trading routes with extreme weather conditions, and the use of lower filling levels.² Lower filling levels evidently lead to an increase in extreme impact events, which have the potential to cause structural damage.^{3,4} Wave impact events are the basis of these extreme loads, which require a fundamental understanding of wave impacts before studying increasingly complex phenomena.⁵

The study of wave impacts on a wall has been an active area of research for decades.^{6–11} Moreover, the impact of waves upon

structures is relevant for many fields such as ocean, coastal, and maritime engineering. Bagnold⁶ already showed significant variation of the wave impact pressure for carefully repeated wave impact experiments. The generation of repeatable waves is not trivial. Small changes in the input parameters, such as the water depth, the wave generation method, and even the weather conditions (for large-scale outdoor experiments), result in significant variability of the impact pressure.^{12,13} On the other hand, the pressure impulse (i.e., the integral of pressure over time) is far more repeatable and is used to model and scale the pressure of wave impact experiments.^{9,10,14–16} In recent years, the study of liquid sloshing^{17–21} and slamming on both wave energy converters^{22–24} and floating offshore structures³ has received considerable attention. The peak impact pressure is especially relevant in these applications.^{3,4}

A number of reviews have been published both on extreme wave impact events and sloshing. For example, the effect of liquid

sloshing impacts has been thoroughly reviewed by Ibrahim.²⁵ A detailed review of water wave impacts on vertical walls is presented by Peregrine,⁴ whereas Dias and Ghidaglia²⁶ presented a detailed review on slamming. The impact of a wave can be divided into several elementary loading processes, such as the direct impact, the jet deflection, and the compression of the entrapped or escaping gas.²⁰ Different types of wave impact can be defined by a combination of elementary loading processes. The classification of wave impact type depends on the wave shape prior to impact, which is either classified as a slosh, a flip-through, a gas pocket, or an aerated type of wave impact.^{4,7,27} For example, the flip-through wave impact has been studied in detail with and without hydroelasticity.^{28,29} The effect of hydroelasticity is relevant for all wave impact types.³⁰ The flip-through wave impact only occurs for a limited parameter space.⁴ On the other hand, the impact of a plunging breaking wave occurs for a wider parameter space and often results in a gas pocket type wave impact. The impact type can easily be identified, but scaling of wave impacts from small-scale to large-scale experiments is not straightforward.

Obtaining dynamic similarity of liquid sloshing or wave impact events is complex.²⁵ The elementary loading processes can be used to identify the required similarity parameters.²⁰ For example, Froude scaling can be used for the global flow, where the wave is not influenced by the presence of the impact wall (i.e., the increase in pressure in the gas pocket and increase in flow from the enclosed gas pocket).^{18,26} The global flow displays remarkable similarities with a plunging breaking wave, which allows for a comparison of the wave crest velocity,^{7,31} the wave crest trajectory,³² and the gas pocket cross-sectional area.^{33,34} The gas pocket behavior *after* wave impact has been studied in detail, which shows that the enclosed gas pocket decreases in volume and starts to oscillate.^{35–37} The decrease in volume of the gas pocket after wave impact is not related to gas leakage at the wave crest.³⁵ On the other hand, the local flow is significantly altered by the strong gas flow over the wave crest for a gas pocket type wave impact. The local flow can be altered by the surface tension of the gas–liquid interface,³⁸ the gas–liquid density ratio,^{39,40} the compressibility of the gas (i.e., the speed of sound),¹⁸ the possibility of phase change,^{5,41,42} and the aeration of the liquid.^{9,43,44} The scaling of the local flow is not well understood, but especially, the formation of ligaments and droplets are thought to be relevant for the variability in wave impact pressures.^{26,45}

The global features of a wave impact on a vertical wall can be accurately represented by potential flow models.^{4,46–49} Apart from ignoring viscous effects, these simulations generally also ignore surface tension effects, as the impact is inertia dominated.⁴⁶ The irrotational flow assumption seems to be valid, as qualitative agreement between experimental and numerical impact pressures can be obtained.²⁶ Nonetheless, the gas phase should not be neglected, especially when the flow separates near the wave crest.⁵⁰ Furthermore, the inertia of the wave tip is small, and consequently, it is pushed upward where it can eventually be blown off the wave crest.^{46,49} Compressible multiphase simulations are required to capture this effect.^{26,51,52} However, the simulations are often not able to capture the development of instabilities on the wave crest.^{24,26,50,53}

The source of impact pressure variability in repeated wave impact experiments is thought to be the instability development on the wave crest. However, the mechanism that is responsible for the formation of these instabilities is still largely unknown.⁴⁵ An

approaching plunging breaking wave that encloses a gas pocket forces a strong gas flow over the wave crest, which results in a shear force on the wave crest. The shear force of the expelled gas is often postulated to result in a Kelvin–Helmholtz type instability.^{40,45,53,54} Additionally, the wave tip of the plunging breaking wave is deflected by the strong gas flow prior to the impact on the wall.^{35,55} Prior to impact, gas cushioning (i.e., the increase in pressure in front of the wave tip) can also result in deformation of the wave tip.^{49,56,57} The wave tip deflection is shown to depend on the density ratio and the scale of the experiment.^{39,40} However, accurate measurements of the wave tip deflection have up to now not been reported.

In the present study, accurate free surface measurements at both the global and local scale were performed to investigate the source of impact pressure variability in repeated wave impact measurements. The variability in impact location of the wave crest is accurately determined, and a mechanism for the development of wave crest instabilities is proposed. Both the free surface instabilities and the deflection of the wave tip are important in the context of sloshing induced loads, where the extreme impact pressure also needs to be taken into account.^{3,4} The global wave behavior is shown to be repeatable for measurements that have negligible system variability. Additionally, the wave behavior prior to impact is shown to resemble a plunging breaking wave. The local flow is investigated with a stereo-planar laser-induced fluorescence (PLIF) technique, which shows both the acceleration and the deflection of the wave tip prior to impact. The wave tip shows a significant variation in impact location on the scale of typical pressure membrane diameters of $d \sim 1$ mm to 5.5 mm.^{19,58} Furthermore, the development of a span-wise instability is observed. The instability on the wave crest is remarkably similar to that of a flapping liquid sheet.⁵⁹ The length scale of the instability depends on the wave shape, density ratio, and the surface tension, which was already suggested in previous work.^{38,40,51,52} Additionally, the study may also provide quantitative data of the wave shape, wave velocity, and wave instability for physical and numerical model validations.

This paper is organized as follows: The experimental setup and equipment are introduced in Sec. II. This section also introduces the experimental procedure required for the generation of repeatable waves. Thereafter, the results are introduced and discussed. First, in Sec. III A, the system variability is quantified and repeatable waves are identified. Then, in Sec. III B, the behavior of the global wave is identified. Finally, in Sec. III C, the local wave behavior is discussed and two sources of impact pressure variability are identified. The findings are summarized in Sec. IV.

II. EXPERIMENTAL APPROACH

A. Wave flume

Figure 1 shows the experimental facility used in this study. The measurements are performed in the wave flume of the Hydraulic Engineering Laboratory at the Delft University of Technology. The flume is 39 m long with a cross section of 0.79×1 m², and the water depth is maintained at $h_0 = 500.0 \pm 0.5$ mm for all measurements. The flume is equipped with a piston-type wavemaker that has a maximum stroke of 2 m. Additionally, the flume contains an active reflection compensation (ARC) system, which is designed to operate during continuous wave or wave spectrum generation. In

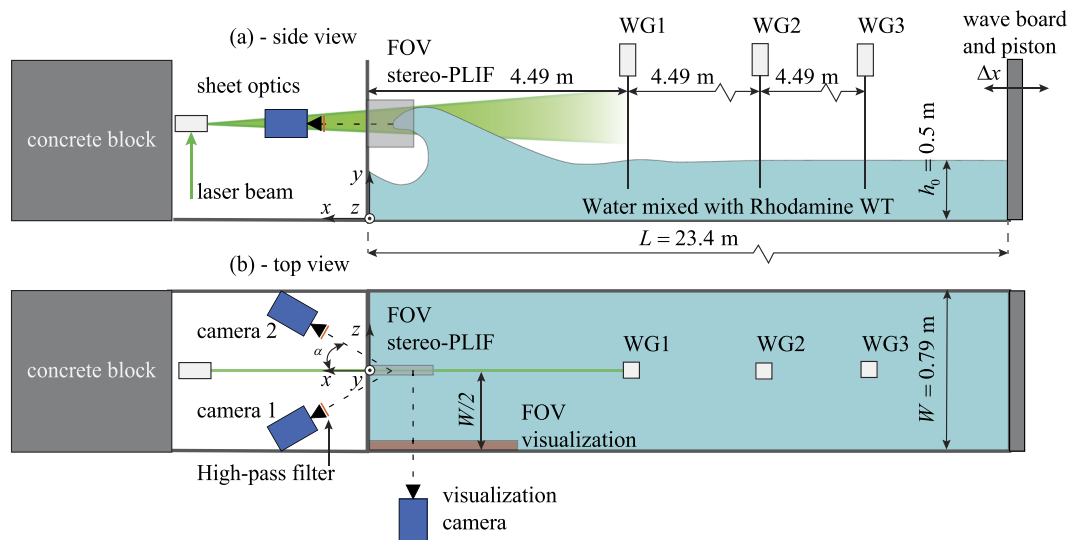


FIG. 1. Schematic of the experimental facility. The origin of the coordinate system is located at the center plane of the wave flume on the bottom of the flume. The positive x -direction is from the wave board toward the impact wall. (a) Side view of the wave flume. The cameras for the stereo-PLIF are aligned on a xz -plane. A vertical light sheet (xy -plane) is created at the center plane of the flume. A focused wave, generated at the wave board ($x = -L$), impacts the impact wall at $x = 0$. (b) Top view of the setup. The visualization camera measures the global wave shape, either at the sidewall or at the light-sheet location. The stereo-PLIF system measures wave crest details in a smaller field-of-view at the light-sheet location.

this work, the ARC system is disabled during generation of the single focused wave. After impact of the focused wave, the system is enabled to dampen the reflected waves and to reduce the downtime between experiments.

The current method of wave generation is similar to the *large scale* tests of the Sloshel project, where the effective flume length is scaled with the length-scale (λ) of the depth-based Froude number (i.e., $\lambda = h_0/H_\lambda = 1/6$, with h_0 being the current water depth and H_λ the being the full-scale water depth).²⁰ A Froude scaled experiment requires a reduced effective flume length, which is obtained by placing a 20 mm thick transparent perspex wall at a distance of $L = 23.4$ m from the wave board (Fig. 1). The perspex wall is attached to a frame, which is fixed to a stable concrete block (i.e., with dimensions of $0.78 \times 0.80 \times 1.00$ m³ and a weight of ~ 1500 kg) placed in the flume. Silicone sealant is applied at the edges of the perspex wall to make it watertight. Nonetheless, exact Froude scaling is not achieved due to practical limitations (e.g., the camera measurement system limits the water depth to 500 mm). The Froude scaled ratio is (1:7.3) compared to the (1:6) ratio of the Sloshel experiments, which will result in a smaller wave (i.e., with a smaller gas pocket and lower wave impact height).^{18,20}

The flume is equipped with a control system, a data acquisition system, resistance-type wave gauges, a position sensor on the wave board, and temperature sensors for both the water and air (TSP01, Thorlabs). The wave shape is additionally determined on a global and local scale with a camera measurement system. The generation of repeatable waves is not trivial, and the required experimental procedure is further detailed in Sec. II D. The wave gauge, position sensor, and trigger signals are collected at a frequency of 100 Hz. The three wave gauges measure the surface elevation ($\eta = y - h_0$) at $x/h_0 = 8.98, 18.0,$ and 26.9 , respectively (Fig. 1). The position sensor

(GHM2000MD601V2 position sensor, Temposonics) records the position of the wave board (Fig. 1).

B. Wave generation

We obtain a large gas pocket wave with a technique that focuses the wave energy in the temporal domain.¹² The wave board (Fig. 1) generates wave groups with their own group velocity and phase speed, which results in a variety of wavelengths, as shown later in Fig. 3. The wave energy of these wave groups is focused on a single location in the flume, the focal point (x_f). The focal point defines the wave shape upon impact, where a shift of the focal point results in respectively: an aerated, a flip-through, a gas pocket, or a slosh impact.⁷ The focal point also determines the angle between the wavefront and the impact wall, where a parallel front (i.e., a wave crest aligned with the impact wall) results in a high impact pressure.⁴⁴ The normalized focal point of $x_f/h_0 = 0.81$ is selected with a trial-and-error approach to obtain a large gas pocket with a parallel front, which results in a spray cloud.⁶

The generation of nominal identical waves with a focusing technique is not trivial, as changes in the initial conditions, such as the water depth, are amplified by the non-linear wave focusing, which results in a different impact type.^{6,13} The variance in impact type results from two sources of variability: the *system variability* and the *hydrodynamic variability*. Minimization of the system variability is essential to study the hydrodynamic variability (e.g., the growth of free surface instabilities on a wave crest). The system variability (i.e., the water depth variation, piston motion variation, and residual motion) is minimized within the limitations of the experimental facility. The comparison between measurements over several days is limited due to inevitable day-to-day variations present in the current

experimental facility.^{13,18} The day-to-day variations are all variations related to water depth, water quality (i.e., natural accumulation of particles on the free surface), and water temperature that cannot be fully controlled in the current facility. The initial water depth variations are expected to be the most significant source of day-to-day variations, as the water depth in this facility could only be set with limited accuracy (i.e., 0.5 mm). Therefore, a single dataset is highlighted, for which the differences in input parameters are carefully reported in Sec. III A.

C. Free surface profile measurement

The wave impact upon a wall displays global and local behavior.¹⁸ The global wave is Froude scaled, whereas hydrodynamic variability alters the local wave behavior. The difference in length scales of the global and local waves require separate measurement systems, which are introduced in Sec. II C 1 and Sec. II C 2, respectively.

1. Global wave profile

A high-speed visualization camera determines the global wave shape (Fig. 1). This CMOS camera (Imager HS 4M, LaVision) is equipped with a 35 mm Micro-Nikkor objective with an aperture number of $f^\# = 8$. Two LED floodlights (ProBeam 170w, Noxion) provide background illumination on a diffusion plate, which for the selected aperture results in good image contrast between the background and laser light (see Sec. II C 2). The field of view is $\sim 353 \times 174 \text{ mm}^2$ at a magnification of $M_0 = 0.06$. The image resolution is reduced to $2016 \times 1000 \text{ pixels}^2$ for a higher camera frame rate (f_{aq}) of 2.5 kHz with an exposure time (Δt_e) of 358 μs , which is sufficiently low to avoid motion blur.

2. Local wave profile

A stereo planar laser-induced fluorescence (stereo-PLIF) technique measures the local wave shape at the center plane of the wave flume. This system is described in detail by van Meerkerk, Poelma, and Westerweel.⁶⁰ The advantage of the stereo camera system is twofold. For a single camera, free-surface measurements can be obstructed by liquid filaments, which is largely avoided by using a stereo-camera system. Second, the stereo camera system enables the use of a self-calibration procedure, which improves the measurement accuracy and reduces alignment errors.⁶⁰

Two high-speed CMOS cameras (Imager HS 4M, LaVision) equipped with 55 mm Micro-Nikkor objectives and a high-pass filter (OG570, Schott) are placed between the impact wall and the concrete block (Fig. 1). The separation angle (2α) of the stereo camera system is $\sim 60^\circ$, with an aperture number of $f^\# = 16$ to accommodate the large separation angle. The image resolution is reduced to 1392×1400 for a higher camera frame rate (f_{aq}) of 2.5 kHz with an exposure time (Δt_e) of 363 μs . The field of view of $150 \times 150 \text{ mm}^2$ aligns with the tip of the focused wave.

The cameras are calibrated with a two-plane dot-pattern target (Type 22, LaVision) with its center at $(x, y, z) = (-104, 730, 2) \text{ mm}$. The bottom corner of the impact wall at the center of the flume defines the origin of the coordinate system and the positive x -direction is defined from the wave board toward the impact wall so that the wave runs with a positive velocity from $x = -L$ to the impact wall ($x = 0$) (Fig. 1). The calibration procedure requires us to

initially image a fluorescent plate to determine a mapping function at the light sheet location. In the following, we often refer to the details of the stereo-PLIF technique described in a previous manuscript.⁶⁰

A light sheet is created from the beam of a Nd:YLF laser (LDY 304 PIV laser, Litron) and focused at the center plane of the flume. The light sheet illuminates the approaching wave, which contains a fluorescent dye at a low concentration (Rhodamine WT, Sigma-Aldrich at 120 mg m^{-3}). The static surface tension does not change at the current fluorescent dye concentration.⁶⁰ The dynamic surface tension is, in some cases, altered by the presence of natural surfactants that settle on the free surface over time (i.e., dust and other natural contaminants).⁶¹ The dynamic surface tension is not determined in the current experiments.

The local wave shape is obtained from the image with the following processing steps (Fig. 2) implemented in Matlab 2020. First, a 3×3 median filter reduces the effects of noise [Fig. 2(a)]. Then, a multi-step edge detection procedure is applied, which uses Otsu's method.⁶² The boundary contour [Fig. 2(b)] is traced after morphological operations are applied to close holes inside the wave shape and to remove small elements outside the wave shape.⁶³ After that, the contour coordinates are mapped using an updated mapping function. A disparity correction is additionally applied to improve the reconstructed profile's accuracy.⁶⁴ Then, a circle [Fig. 2(c)] is fitted to the edge of the gas pocket.⁶⁵ Thereafter, the profiles of both cameras are combined by averaging over the k -nearest neighbor of camera 1 with respect to camera 2, with a limit of $D_l = 2.5 \text{ mm}$ on the point distance [Fig. 2(d)].⁶⁶ Finally, the combined profile is cropped to remove the image boundaries at the minimum y -coordinate of the circle fit and the minimum x -coordinate of both camera profiles.

The measurement accuracy of the stereo-PLIF system is determined for the initial calibration and a typical wave crest (i.e., free surface profile). First, the initial mapping function is determined with an accuracy of $\sim 0.06 \text{ mm}$ (e.g., 0.3 pixels and 0.8 pixels for the x - and y -coordinates, respectively). The camera perspective results in a significant variation of the resolution (S).⁶⁰ The resolutions over the x (S_x) and y (S_y) coordinate are $4.9 \text{ pixels mm}^{-1}$ and $13 \text{ pixels mm}^{-1}$, respectively. Second, a systematic error is introduced when the free surface profiles from the two cameras are combined. This systematic error is defined as the average Euclidean norm (L_2) between the combined and individual profiles. The systematic error for a typical free surface profile [Figs. 3(e) and 3(f)] is $\sim L_2 \approx 0.35 \text{ mm}$ (e.g., ~ 1.7 pixels or 4.6 pixels based on the x - and y -coordinates, respectively, of the initial mapping function). The systematic error is larger at the top of the wave crest ($L_2 \approx 0.5 \text{ mm}$) where the light sheet skims over the wave surface (see Sec. III C), which results in an increase in the measurement uncertainty. The measurement accuracy is mainly defined by the systematic error, whereas the error of the initial calibration appears to be negligible.

D. Experimental procedure

Nominal identical waves require a repeatable experimental procedure. The steps in the procedure are detailed in this section, which describes the residual motion reduction, water level control, and measurement procedure.

The free surface is disturbed by waves at several moments during a measurement. The waves are introduced when the wave board

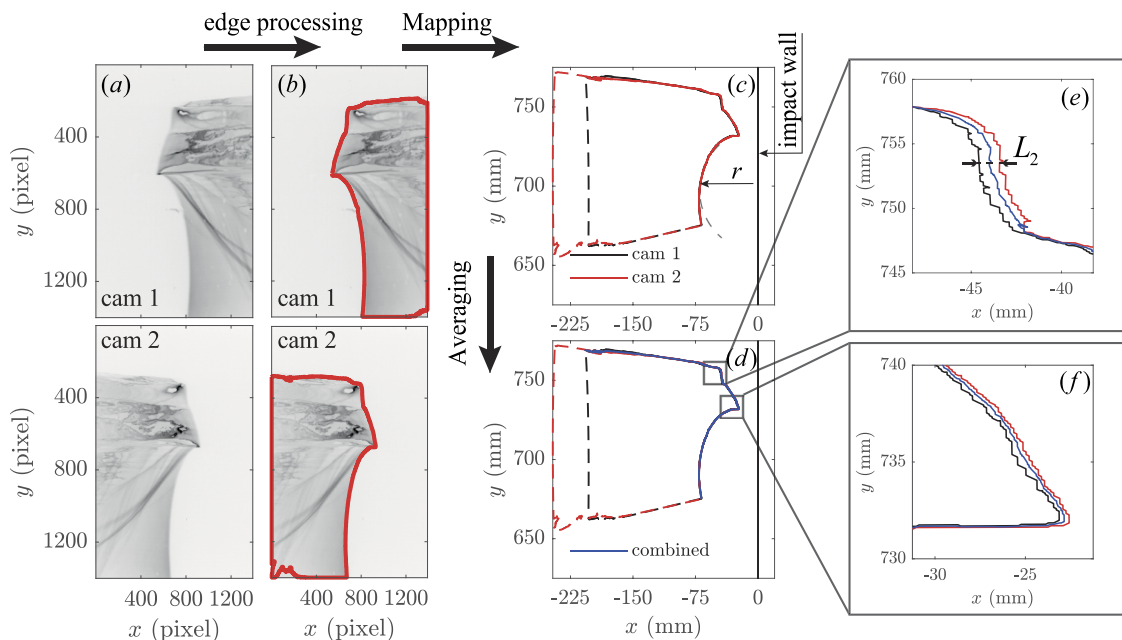


FIG. 2. Data processing steps for the stereo-PLIF for the present measurements. (a) The original image pair from cameras 1 and 2 (Fig. 1). (b) The free surface profile after edge processing. (c) The profiles of both cameras mapped to world coordinates. The valid free surface profiles are indicated by a continuous line, whereas the invalid parts of the free surface reconstruction (i.e., the image borders) are indicated by a dashed line. The impact wall is located at $x = 0$ and the wave approaches the wall (i.e., from negative x that is defined to point toward the wave board). (d) The final combined profile based on the k -nearest neighbor search with insets (e) and (f) showing the typical variance of the averaged profile with respect to the separate camera profiles as the distance norm of $L_2 \approx 0.5$ and $L_2 \approx 0.2$ mm for panels (e) and (f), respectively.

of the flume is zeroed or when the water level is adjusted. The waves that reflect from the impact wall also disturb the free surface. This residual motion of the free surface is removed with the ARC by enabling it for 7 min, which based on previous experiments significantly reduces the free surface fluctuations.⁶⁷ The ARC is disabled after the allotted time, and the water is left untouched for 7 min. However, the longest standing wave (i.e., seiche wave) is not completely attenuated by the bottom friction, which would require an impractically long downtime between measurements.^{13,67} Despite this, the procedure reduces the free surface fluctuations within acceptable limits for the present experiments.

The water level is checked with a ruler before the start of a measurement. Additionally, the water level is monitored with higher precision with the visualization camera (see Sec. III A). The resolution of the ruler is 0.5 mm, which defines the minimum threshold for the water depth change. The water level is adjusted when the threshold is exceeded, and thereafter, the residual motion is reduced according to the experimental procedure described above.

The measurement procedure initiates with the start of the acquisition devices and wave generation. These are separate systems where the programming timing unit (PTU) of the camera system is used as a master clock during the measurements. The camera and analog acquisition system are both enabled prior to wave generation.

The analog acquisition system is manually enabled and collects data from the wave gauges and piston position sensor at a frequency of 100 Hz. Additionally, the trigger signals from both the wave

generation and the camera acquisition system are recorded. The data of the analog system are matched to the master clock based on the trigger signal of the wave generation system.

The camera acquisition system acquires data at a frequency of 2.5 kHz in a ring buffer, which enables continuous recording. This ring buffer allows a remote signal to trigger the recording of the camera measurement system. The remote trigger signal is sent from a delay generator (digital delay generator DG535, Stanford Research Systems), which in turn is triggered by the wave flume.

The wave generation system is manually activated to generate a single focused wave. The wave generation system sends a trigger signal to both the camera and analog acquisition systems. Finally, the acquisition system is disabled after wave impact and the experimental procedure is repeated.

III. RESULTS AND DISCUSSION

A. System variability

On a global scale, the wave is considered repeatable for the current facility when the system variability is minimal within the practical limitations. In this section, the wave-gauge signal, piston motion, and still-water level are analyzed for 12 selected measurements. These 12 measurements are part of a set of 32 measurements, obtained over multiple days. The analyzed measurements were performed on the same day to avoid day-to-day system variability.

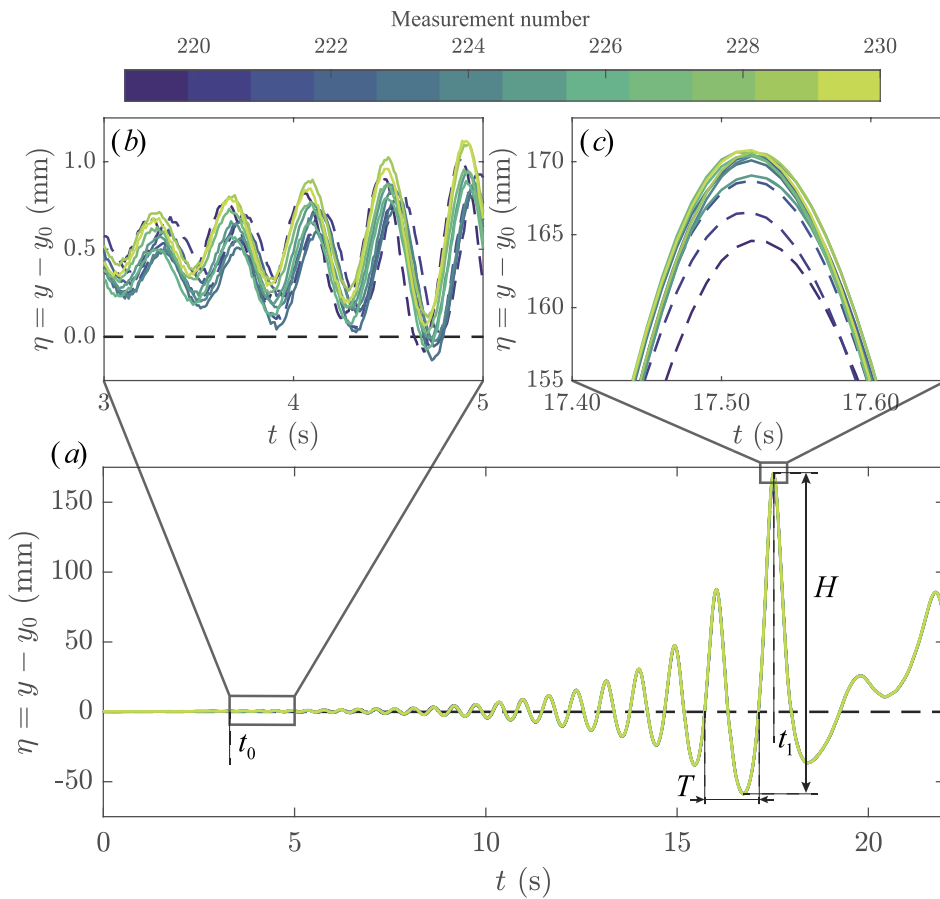


FIG. 3. (a) The wave elevation signal at wave gauge 1 (WG1 in Fig. 1) is shown for 12 measurements obtained on the same day with an initial water depth of $h_0 = 500$ mm. The still-water level (y_0) of the wave gauges is subtracted from surface elevation signal (y). The amplitude (H) and period (T) of the highest wave are also defined. The continuous lines show repeatable measurements, whereas dashed lines indicate outliers identified based on the amplitude of the highest wave. The difference between repeatable and non-repeatable (i.e., outlier) waves is highlighted in panels (b) and (c), where a zoomed-in view of the free surface elevation signal is shown for the short and long waves, respectively.

The water quality (in particular, the surface tension) is assumed to be constant, and the water temperature variation ($\Delta T = 0.3^\circ\text{C}$) is considered negligible.

The wave shape and wave height change significantly for small water depth variations (i.e., a water depth variation larger than 0.15% of the initial water depth is significant).^{13,67} An estimate of the water depth variation is determined from samples ($N = 100$) of the still-water level that were recorded prior to each measurement. A line is fitted through the still-water level, which shows a variation in initial water depth of $\Delta h_0 = 0.08$ mm with a bias of 0.15 mm with respect to the linear fit of the still-water level. The water depth variation is

lower than 0.15% of the initial water height. Therefore, the influence of the initial water height on the system variability is negligible for the measurements performed on a single day.⁶⁷

The piston motion (x_p) and wave-gauge signal (η_{WG1}) are compared with methods commonly used to quantify the repeatability of focused waves.^{11,12,18} The height (H) and last zero up crossing period (T) of the highest wave are determined for both the piston motion and free surface elevation (Fig. 3). For both signals, the mean (μ), standard deviation (σ), and coefficient of variation ($c_v = \sigma/\mu$) are reported (Table I).^{12,18} Additionally, the peak root-mean square error (RMSE) is defined.¹¹ Finally, the coefficient of

TABLE I. The system variability is based on repeatability estimates of the piston motion (x_p) and the free surface elevation at wave gauge 1 (η_{WG1}). The free surface elevation without outliers (η_{WG1}^*) is also reported.

| Case | Number of measurements | E_s ($\text{mm}^2 \text{s}$) | | | H (mm) | | | T (s) | | |
|----------------|------------------------|----------------------------------|-------|----------|-----------|-------|-------------------------|-----------|--|--|
| | | c_v (%) | μ | σ | c_v (%) | μ | $\sigma \times 10^{-3}$ | c_v (%) | | |
| x_p | 12 | 0.4 | 213.1 | 0.21 | 0.10 | 2.1 | 0.30 | 0.01 | | |
| η_{WG1} | 12 | 1.2 | 227.9 | 2.1 | 0.92 | 1.41 | 0.74 | 0.05 | | |
| η_{WG1}^* | 9 | 1.0 | 229.1 | 0.21 | 0.09 | 1.41 | 0.58 | 0.04 | | |

variance for the energy of the piston motion signal [$E_s = \int_{t_0}^t |x(t)|^2 dt$] is computed.¹⁸

The period of the highest wave is repeatable for both the piston motion and free surface elevation, with an insignificant standard deviation compared to the resolution of the acquisition system (i.e., $\Delta t = 10$ ms). The period of the highest wave is reduced as the wave steepens.

The piston motion is also highly repeatable, with a negligible standard deviation compared to the resolution of the acquisition system (i.e., 0.21 mm is equivalent to 2.1 mV). The variation in the signal power (E_s) is also insignificant (Table I).

Figure 3 shows the free surface elevation signal for the reported experiments, where the insets highlight the small amplitude (b) and large amplitude (c) free surface waves. Colors represent the different repetitions of the experiment. The numbering is kept consistent within the larger experimental campaign for data reusability. The standard deviation of the peak height is not negligible compared to the free surface elevation (η_{wg}), and outliers (dashed lines) can easily be identified for the highest wave [Fig. 3(c)]. The outliers are based on the median absolute deviation (MADe). A significant reduction in the standard deviation and coefficient of variation of the wave height are obtained with only the repeatable waves (η_{wg}^*). A possible source of the wave height variation is a remaining free-surface fluctuation (i.e., a seiche wave) at the start of the measurement.⁶⁷ The coefficient of variation of the piston motion is low and does not depend on the repeatable and non-repeatable waves. The combined repeatability measures indicate insignificant system variability, and consequently, the global wave is expected to be well repeated.^{12,13,18}

B. Global wave behavior

The analysis of the system variability indicates that the wave generation is repeatable for the nine selected waves from a set of 12 measurements (Table I). Now, the images obtained with the visualization camera are analyzed to compare the repeatability of the

generated waves. First, the global wave behavior is visually compared. Then, the shape of the gas pocket and the location of the wave tip are determined. Finally, the cross-sectional area of the gas pocket in the plane of observation is determined, and an estimate of the local gas velocity at the wave crest is derived.

1. Visual comparison

The qualitative repeatability is determined with a visualization camera by comparing differences in image intensity.³⁸ Here, the global wave shape, as obtained with the visualization camera, is compared for two typical measurements (M225 and M228) shown in panels (a) and (b) of Fig. 4. The red (M225) and cyan (M228) highlights show the difference in image intensity between both measurements at two time steps $t = -28.0$ ms and $t = -16.0$ ms with respect to the time of impact ($t = 0$ ms). The wave crest development for a typical wave (i.e., M225) can be observed at different time steps in the supplementary material.

The free surface is determined at the side wall of the wave flume, where the width of a color band (i.e., red and cyan areas) is a measure of the differences in the global wave shape. The width is estimated at the tip of the wave crest [Fig. 10(c)] and the bottom of the trough [Fig. 10(d)]. The difference in global wave shape is on average $L_2 \approx 4.4$ mm for $t = -16.0$ ms at the indicated regions. Although, these results must be interpreted with care, as variations in image intensity arise from multiple sources (e.g., laser-intensity fluctuations and a wetted or unwetted side wall). The overall shape of the global wave is quite similar. However, a more detailed analysis should be performed, as the variability in impact pressure is also related to small variations in the gas pocket shape.⁷

2. Cross-sectional shape of the gas pocket

Initially, the focused wave resembles a plunging breaker, which is used to define the gas pocket shape. The area of the gas pocket is

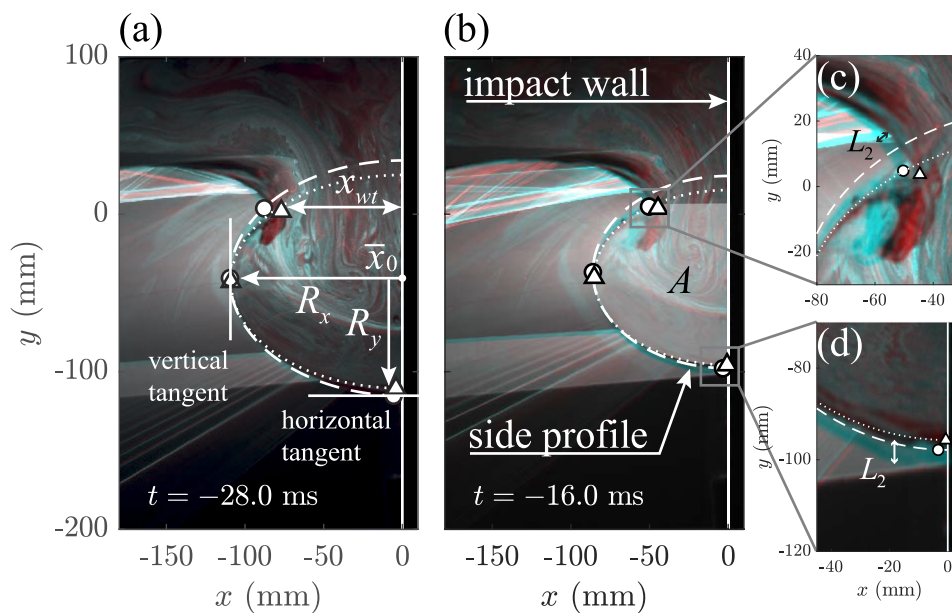


FIG. 4. [(a) and (b)] The back-projected side-view images of two nominal identical waves are superimposed at two time steps, where differences in intensity are indicated in red (M225) and cyan (M228). The colors highlight the variance in wave shape. The striations behind the wave crest result from refraction of the light sheet at the wave crest and are measure of the subpixel variations present on the wave crest. Additionally, the semi-ellipse fit of the gas pocket is shown for M225 (dotted line) and M228 (dashed-dotted line). The wave crest (\bar{x}_{wt}), ellipse center (\bar{x}_0), and the ellipse's semi-major and semi-minor axes (R_x , R_y) are defined in window (a). The cross-sectional area (A) of the gas pocket is defined in panel (b). The panels (c) and (d) show the intensity variation between waves with an averaged free surface variation of $L_2 \approx 5.0$ mm and $L_2 \approx 3.8$ mm, respectively.

typically reported at the moment of impact or during the compression cycle, where the gas pocket cross-sectional area is either fitted with a semiellipse³⁶ or as a semicircle.^{11,18} The area underneath a plunging breaker can also be approximated by an ellipse with a constant aspect ratio,³³ but the accuracy of this ellipse fit is a subject of debate for a plunging breaker.³⁴ Here, the gas pocket cross-sectional area is fitted with a semiellipse constrained to the impact wall.

The parameters of the ellipse (i.e., the semi-major axis R_x , the semi-minor axis R_y , and the center-point \bar{x}_0) are defined in panel (a) of Fig. 4. The ellipse semi-axes are manually determined using the images of the visualization camera, where the ellipse axes tend to correspond to the horizontal and vertical tangent of the gas pocket [Figs. 4(a) and 4(b)]. The ellipse center is defined by the x -location of the wall and additionally the y -location of the vertical tangent. The location of the tangent (i.e., vertical and horizontal) is manually estimated. The manual estimate is improved by detecting the maximum intensity gradient over a line perpendicular to the tangent.

The semi-ellipse fit overlaps with the cross-sectional area of the gas pocket of the visualization camera, as shown in panels (a) and (b) of Fig. 4. However, small differences are observed near the wave crest and in the trough of the gas pocket (Fig. 4). The manual selection accuracy over repeated evaluations is ~ 0.3 mm and 2.2 mm (i.e., equivalent to 0.5% and 5.4% of the semi-major and semi-minor axes, respectively, for a typical gas pocket at the moment of impact) for the R_x and R_y axes, respectively. The uncertainty in the R_y component is larger due to the reduced image intensity at the horizontal tangent of the gas pocket [Fig. 4(b)]. This results in a variation of R_y over repeated experiments, as shown in Fig. 5.

The semi-major and semi-minor axes are approximated by a linear function (Fig. 5). The upward motion of the wave trough (i.e.,

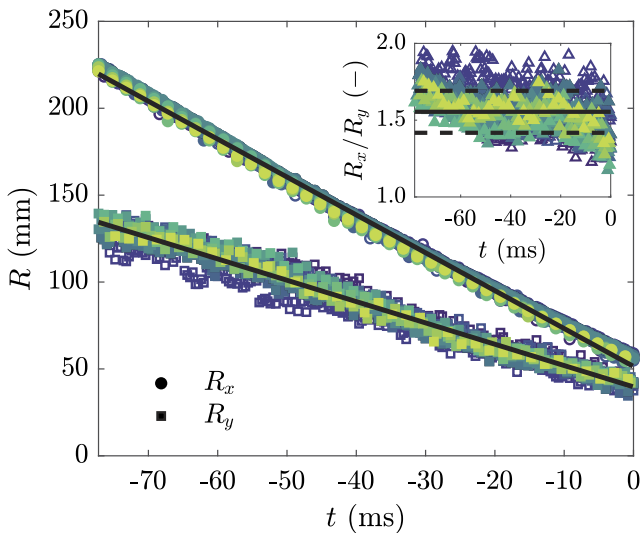


FIG. 5. The semi-major (R_x) and semi-minor (R_y) axis of the fitted ellipse for the characterization of the observed gas pocket (see Fig. 4) are shown, where the open markers define the non-repeatable waves of Fig. 3. The semi-minor and semi-major axis are approximated by a linear fit $R_y = -1.23t + 39.7$ and $R_x = -2.18t + 51.4$. The inset shows a nearly constant aspect ratio of $R_x/R_y \approx 1.6 \pm 0.1$ (for $-60 \leq t \leq 20$ ms).

the contact point of the wave and the wall) is defined by the derivative of the semi-minor axis (\dot{R}_y) and is \sim constant at -1.23 m s⁻¹. The wave speed is defined by the derivative of the semi-major axis (\dot{R}_x) and is conjectured to change. The wave speed is initially 2.38 m s⁻¹ for $-80 \leq t \leq -40$ ms, but it decreases to 2.00 m s⁻¹ for $-40 \leq t \leq 0$ ms. The averaged wave speed is 2.18 m s⁻¹, which is approximately equal to the shallow water phase speed ($\sqrt{gh_0} \approx 2.21$ m s⁻¹). The aspect ratio of the ellipse is nearly constant at $R_x/R_y = 1.6$ for $-60 \leq t \leq -20$ ms, which approximates the aspect ratio of $\sqrt{3}$ for plunging breakers.^{33,34,68} The velocity ratio is also relatively constant, which results in a velocity \dot{R}_y of approximately $\sqrt{gh_0}/3$.

The repeatability of the global wave is determined from the ellipse fit. First, the systematic error with respect to the linear fit is defined per measurement, which is on average 0.8 mm and 3.6 mm for the semi-major (R_x) and semi-minor (R_y) axes, respectively. A measure of the wave shape repeatability is the random error, which is on average 1.1 mm and 1.7 mm for both axis. The higher random error of the semi-minor axis is a result of the detection method. Small variations in gas pocket size are a source of variability in impact pressure.⁷ However, the random error is negligible (i.e., 2.0% and 4.2% of a typical gas pocket at the moment of impact); as such, the global wave shape appears to be repeatable based on the gas pocket size.

3. Wave tip

The development of the plunging wave tip is determined from the images of the visualization camera. The wave tip is formed when the gradient of the free surface profile is large, which results in a pressure gradient in the fluid that accelerates a liquid jet horizontally.³² The wave tip becomes thinner and longer while following a ballistic trajectory.³² In the present measurements, the wave tip does not follow a ballistic trajectory, as the cross flow at the wave tip results in a drag force that counteracts the gravitational force.

The wave tip trajectory is determined with the detection method previously used for the ellipse axes. The tip coordinate is determined for every fifth time step ($\Delta t = 2.0$ ms), which is sufficiently small to determine the global wave tip behavior. The wave tip is detected with an accuracy of ~ 0.96 mm and 0.31 mm for the x and y -coordinates of the wave tip, respectively. Figure 6 shows the wave tip trajectory for both the x - (x_{wt}) and y -coordinate (y_{wt}).

The wave tip trajectory appears to be nearly linear for both coordinates (Fig. 6). The residual error of the linear fit is 3.6 mm and 2.1 mm for the x and y -coordinates, respectively, which indicates repeatable wave-tip behavior. Furthermore, there is no clear distinction in wave tip behavior between the previously defined repeatable and non-repeatable waves.

The components of the wave tip velocity are $\dot{x}_{wt} = 2.67$ m s⁻¹ and $\dot{y}_{wt} = 0.1$ m s⁻¹, which results in a rising wave tip as it approaches the impact wall. The ratio of wave tip and global wave velocity $\dot{x}_{wt}/\sqrt{gh_0}$ is ~ 1.22 , which is similar to the velocity ratio of a plunging breaker.⁷ The wave tip trajectory deviates from the linear fit for $-20 \leq t \leq 0$ ms, which indicates an acceleration of the wave tip during the final stage before impact. The acceleration of the wave tip is approximately $a \sim 100$ m s⁻² based on $a \sim (2\Delta x)/\Delta t^2$ with $\Delta x \approx 15$ mm with respect to the linear fit of x_{wt} and $\Delta t \approx 18$ ms for $-19.2 \leq t \leq -1.2$ ms (Fig. 6).

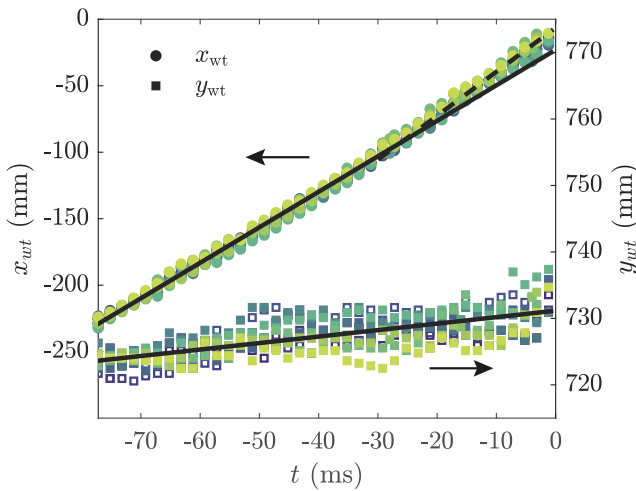


FIG. 6. The wave tip coordinates (x_{wt} , y_{wt}) obtained with the manual fitting procedure from the visualization camera. The tip coordinate is approximated by a linear function in both $x_{wt} = 2.67t - 22.97$ and $y_{wt} = 0.10t + 731.2$. The closed markers indicate repeatable waves, based on the surface elevation data, whereas the open markers indicate non-repeatable waves.

4. Gas pocket cross-sectional area

Small variations in the gas pocket shape can result in impact pressure variability.⁷ The gas pocket cross-sectional area is determined to define the global wave shape repeatability and estimate the local gas velocity in front of the wave crest. The variability in impact pressure due to the variation in gas pocket size is expected to be minimal, as the ellipse axis and wave-tip coordinate already indicate a repeatable global wave behavior. The gas pocket cross-sectional area is defined as the ellipse segment *underneath* the wave crest tip,

$$A = \frac{1}{2}(\pi R_x R_y - A_s), \quad (1)$$

with A_s being the area of the elliptical segment *above* the wave crest tip. The area of the elliptical segment is defined as follows:

$$A_s = R_x R_y \left[\arccos \left(1 - \frac{h}{R_y} \right) - \left(1 - \frac{h}{R_y} \right) \sqrt{2 \frac{h}{R_y} - \frac{h^2}{R_y^2}} \right], \quad (2)$$

with $h = R_y - (y_{wt} - y_0)$ being the sector height of the elliptical segment (Fig. 4). Figure 7 shows the calculated gas pocket cross-sectional $A - A(0)$ area, where the value at impact (A_0) is subtracted. The gas pocket cross-sectional area at impact is $\sim 4.1 \times 10^3 \text{ mm}^2$ with a standard deviation of 6.5%. The power of the best fit function to the gas pocket cross-sectional area is 1.52, which is $\sim 3/2$, as shown in the log-log inset of Fig. 7. Furthermore, the non-repeatable waves, based on the free surface elevation, are indistinguishable from the results for the repeatable waves.

The gas velocity at the wave crest increases as the wave approaches the wall. The incompressible gas velocity at the wave crest (V_g) follows from a control-volume attached to the ellipse,

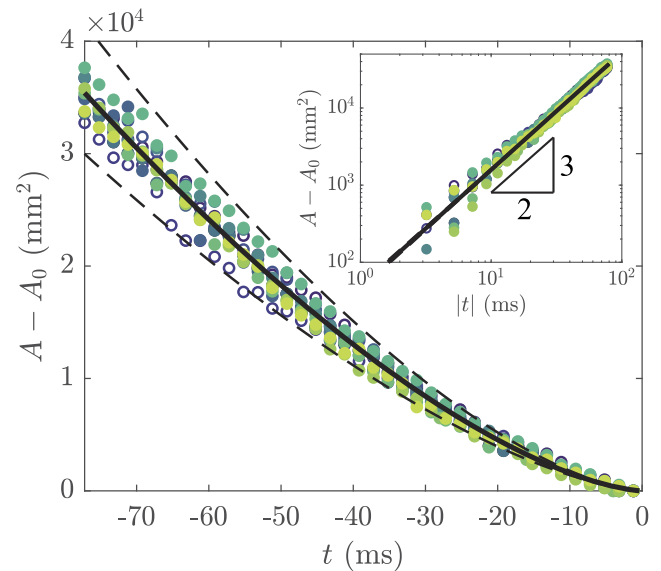


FIG. 7. The gas pocket cross-sectional area is the area enclosed by the wave tip and the ellipse [Fig. 4(b)]. The gas pocket cross-sectional area is approximated by a power-law $A(t) - A(0) = 1.74|t|^{1.52}$, which is shown in the log-log inset.

$$V_g = \frac{1}{\Delta x} \dot{A} \sim |t|^{-0.48} \sim |t|^{-1/2}, \quad (3)$$

where $\Delta x = \dot{x}_{wt} t \sim 1.2\sqrt{gh_0}t$ is the distance between the wave crest and the wall and $\dot{A} = 2.64|t|^{0.52} \sim 1.2\sqrt{gh_0}|t|^{1/2}$ is the temporal derivative of the cross-sectional area of the gas pocket. The gas can be considered as incompressible for a Mach number ($M = V_g/c$) lower than 0.3. The gas in the cavity is incompressible for $V_g = |t|^{-1/2} = 0.3c$ or up to $|t| = (0.3c)^{-2} \approx 0.09 \text{ ms}$, where c is speed of sound (343 m s^{-1} at standard conditions). The gas velocity at the wave crest ranges from $3.5 \leq V_g \leq 15.8 \text{ m s}^{-1}$ for $-80 \leq t \leq -0.4 \text{ ms}$. The global wave does not appear to decelerate through compression of the gas pocket.

C. Local wave behavior

The variation in impact pressure of nominal identical waves is caused by the development of free surface instabilities on the wave crest.^{26,45,54} Here, a stereo-PLIF system is used to accurately measure the free surface of the wave crest and to determine both the development of instabilities and the wave tip deflection. The wave crest is determined with a smaller field-of-view than the visualization camera, which results in a higher resolution and accuracy of the free surface measurements. The system enables free surface measurements in the center plane of the wave flume where side-wall effects (i.e., friction⁵⁸ and wetting⁶⁷) do not directly influence the measurement of the wave shape. First, the visualization camera and stereo-PLIF system are compared. Then, the temporal development of a local wave crest is discussed both in the context of measurement accuracy and wave tip behavior. Thereafter, the free surface profile is compared over several time steps. Finally, the wave tip and the variability due to variations in the wave shape are discussed.

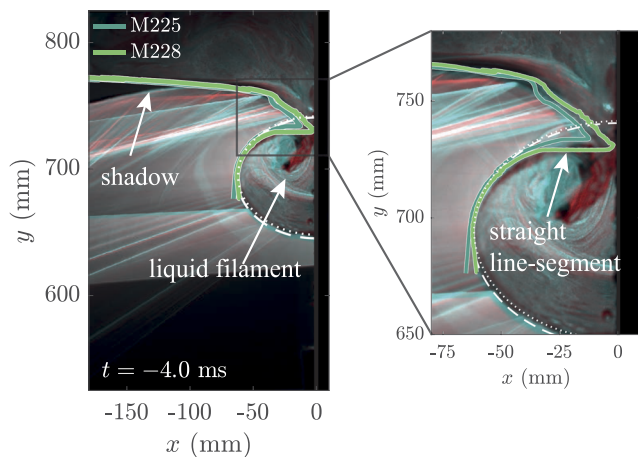


FIG. 8. The side-view images of two nominal identical waves are superimposed for $t = -4.0$ ms and combined with the free surface profile from the stereo-PLIF measurement (continuous line). The ellipse fit from the visualization camera is also included. The refraction of the light sheet at the wave crest results in striations. These striations present a sub-pixel measure of the wave crest variability. However, they are neglected when comparing the visualization and stereo-PLIF measurements. A zoomed-in view on the wave crest shows the difference between both waves and the formation of liquid filaments at the sidewall.

1. Global and local measurements

The stereo-PLIF data of two typical measurements (e.g., M225 and M228) are compared with the images of the visualization camera that are obtained simultaneously (Fig. 8). The stereo-PLIF results are superimposed (continuous line) on the combined side-view images of the visualization camera by matching the origin of both coordinate systems. The ellipse fit (dashed and dotted line) is also included, which shows a qualitative agreement with the stereo-PLIF results.

The wave-crest profile at the center plane (stereo-PLIF data) is similar to that at the side wall (visualization data). The large field-of-view of the visualization camera combined with the relatively small focal length lens results in a perspective view of the wave crest, which emphasizes the spanwise differences of the wave crest (see the [supplementary material](#)). For example, a liquid filament is suspended

from the wave crest at the side-wall, whereas the filament is absent on the rest of the wave crest (i.e., the spanwise direction). The side-wall effects, such as friction⁵⁸ and wetting,⁶⁷ limit the use of side-view measurements for quantitative repeatability studies of the wave tip behavior.

The application of a stereo-PLIF system in the wave flume is not without problems. For example, the liquid exerts a large pressure on the wall when it impacts, which results in vibrations in the camera system. The vibrations can introduce a misalignment in the camera system, and a self-calibration procedure is needed to correct for the misalignment.

Additionally, loss of information occurs when a free surface undulation casts a shadow. This effect is observed at the top of the wave crest where the light sheet skims over the free surface and obstructs the backward side of the wave (Fig. 8). The wave tip also blocks the inside of the gas pocket as it plunges over the top. A straight line results at the blocked segment, which connects the wave tip and the backward face of the gas pocket (Fig. 8). The wave tip is accurately determined by the light-sheet cutoff, whereas the accuracy decreases at the wave top.

The stereo-PLIF system enables a quantitative comparison of repeated measurements, whereas the side-view camera only enabled a qualitative comparison. A zoomed-in view of the free surface profile shows the difference between two selected measurements M225 and M228 [panels (c) and (d) of Fig. 4]. The averaged difference between the free surface profiles as determined by the stereo-PLIF measurements is $L_2 = 2.45 \pm 1.49$ mm over the entire field-of-view. The difference was previously determined to be $L_2 = 4.4$ mm for $t = -16.0$ ms based on the visualization camera. The quantitative difference determined with the stereo-PLIF measurements is lower, even for a later time step. The stereo-PLIF and visualization measurements show that the wave is repeatable on a global scale.

2. Temporal development

Figure 9 shows the temporal development of the free surface for a typical case (M225) at two different time steps, which show the local ($\Delta t = 0.8$ ms) and detailed ($\Delta t = 0.4$ ms) free surface behavior. The *local wave behavior* shows the displacement of a small amplitude *liquid jet*, which is initially ejected from the wave crest (e.g., outside of the field-of-view of the stereo-PLIF measurements), as shown

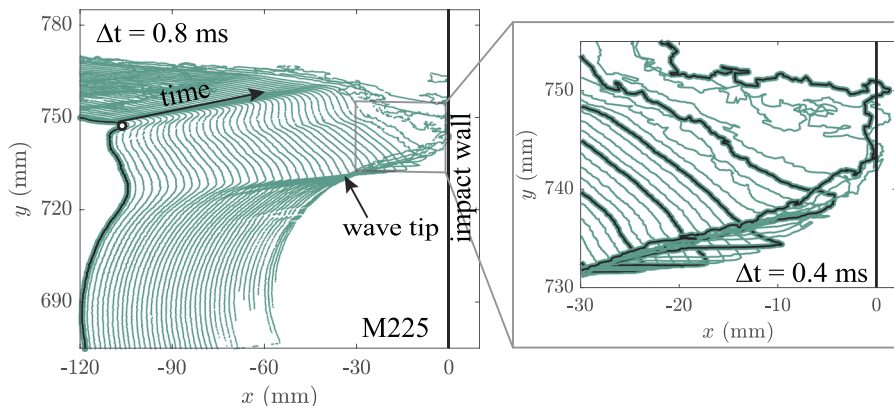


FIG. 9. The free surface stereo-PLIF data for experiment M225 is consistent over multiple time steps ($-29.6 \leq t \leq 2.8$ ms) at a reduced temporal resolution ($\Delta t = 0.8$ ms). The marker shows the location of the *liquid jet* that is initially ejected outside the field-of-view of the stereo-PLIF measurement (see the [supplementary material](#)). The zoom shows the free surface stereo-PLIF data at its actual temporal resolution for $-7.2 \leq t \leq 2.8$ ms with an increased line width for every fourth time step.

in the [supplementary material](#). The disturbance (i.e., the *liquid jet*) is displaced to the back of the wave crest by the gas flow over the wave crest. The growth and displacement of the disturbance are continuous over time, which is indicative of the temporal consistency of the stereo-PLIF data (e.g., the initial disturbance is physically there).

The details of the wave crest moments before impact are displayed in panel (b) of [Fig. 9](#). Initially, a liquid jet is ejected from the wave crest as the gradient of the free surface profile increases, which results in a large pressure gradient in the fluid.^{32,68} In this measurement, a liquid jet is ejected two times, which results in the initial disturbance (i.e., defined by the marker) and the wave tip. The wave tip of a plunging breaker follows a ballistic trajectory, but here, the wave tip is displaced upwards by the air flow from the gas pocket. The gas velocity at the wave crest increases as the wave approaches the wall, which results in a wave tip that is stretched and deflected.⁵¹ The formation of spray (i.e., droplets) and ligaments results in a higher noise level in the stereo-PLIF data, which is observed in the last few time steps of panel (b).

3. Local repeatability

In the previous analysis of the system variability, several repeatable and non-repeatable waves were identified. The stereo-PLIF data for both the repeatable and non-repeatable waves are presented ([Fig. 10](#)). The waves initially ($t = -28.0$ ms) overlap, and the variation increases as the waves approach the wall. The variability concentrates in the vicinity of the wave tip for all waves. Initially, the formation of instabilities is not observed, both in the processed free surface profile and in the original shadowgraph of the stereo-PLIF images. However, at later stages [[Fig. 10\(c\)](#)], the wave tip is deflected differently. This is hypothesized to be caused by an interaction of the gas flow and interface around the wave crest.

The variability of the free surface profiles is quantified. First, the difference in wave crest height ($-120 \leq x \leq -115$ mm) is determined

from stereo-PLIF data at $t = -28.0$ ms [[Fig. 10\(a\)](#)]. The standard deviation in the height of all waves is ~ 1 mm, whereas the nominal identical waves show a standard deviation of ~ 0.9 mm. The difference between both sets (i.e., repeatable and non-repeatable waves) is negligible, which is also confirmed by the initial visual overlap of all waves [[Fig. 9\(a\)](#)]. However, the variation in free surface profile is more significant at the wave crest (i.e., $730 \leq y \leq 740$ mm) for $t = -28.0$ ms with a standard deviation of ~ 3.5 mm.

A parametric representation of the free surface profiles is determined with an arc-length method. The curve is parameterized with a fixed number of elements ($N = 2500$), which results in a spacing of ~ 0.15 mm. A Euclidean distance metric (L_2) is computed from the difference between parametric curves and their respective averaged free surface profile. The distance metric increases from approximately $L_2 = 1.5$ mm at $t = -28.0$ ms to $L_2 = 5.1$ mm at $t = -16.0$ ms and to $L_2 = 8.0$ mm at $t = -4.0$ ms. The Euclidean norm (L_2) confirms the buildup of variability in the wave shape as the wave approaches the wall. The variation is most obvious at the wave tip, whereas the global wave (i.e., the wave top and the wave trough) remains similar, which is additionally supported by the movie in the [supplementary material](#).

The wave tip variation is further investigated to determine its possible effect on the pressure variability, where the extreme position of the wave tip is defined as the maximum x -location of the stereo-PLIF profile ([Fig. 11](#)). First, the wave tip velocity in the x -direction $\dot{x}_{wt} = 3.31 \text{ m s}^{-1}$ is higher than previously determined from the visualization camera, $\dot{x}_{wt} = 2.66 \text{ m s}^{-1}$. A deviation from the linear fit was already observed for $-20 \leq t \leq 0$ ms, which indicated an acceleration of the wave tip. However, the wave tip was, for $-20 \leq t \leq 0$ ms, obscured by either the perspective of the visualization camera or the formation of a liquid filament at the side wall. The wave tip velocity in the x -direction is significantly higher $\dot{x}_{wt} \sim 1.5\sqrt{gh_0}$ for $-20 \leq t \leq 0$ ms, which is higher than the wave tip velocity of a plunging breaker ($\dot{x}_{wt} \sim 1.2\sqrt{gh_0}$).⁷ However, the wave tip velocity in the x -direction is comparable to that of a plunging breaker that impinges

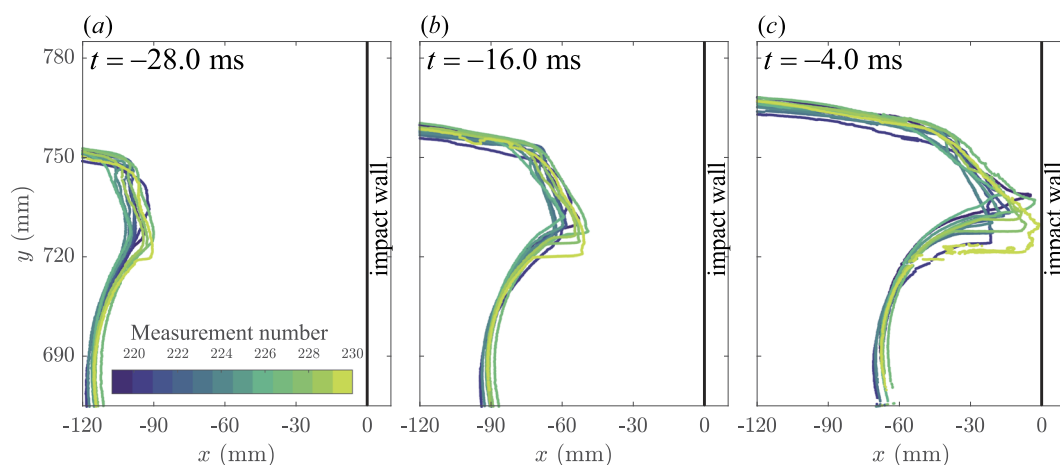


FIG. 10. The stereo-PLIF data of all 12 measurements for three time steps, and additionally, a movie of the wave crest development is available as the [supplementary material](#). [(a) and (b)] Initially, all 12 measurements tend to overlap. (c) The overlap between the different measurements reduces significantly as the waves approach the wall. The variation in free surface profile concentrates near the wave tip, which is influenced by an increase in gas velocity.

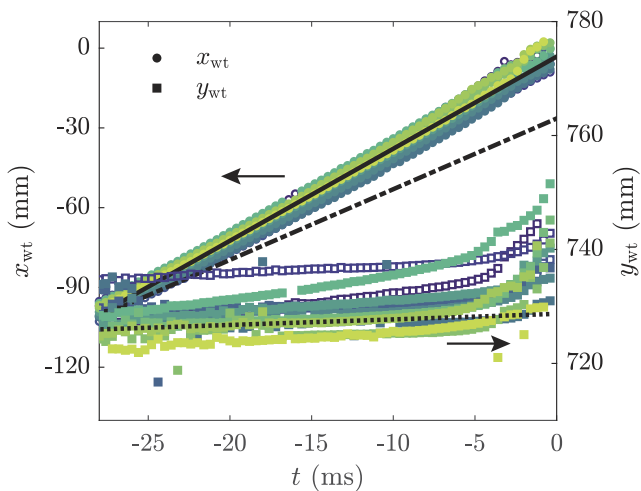


FIG. 11. The wave tip coordinates for $-28 \leq t \leq 0$ ms obtained from the stereo-PLIF data. The wave tip coordinates are initially fitted with a linear function $x_{wt} = 3.31t - 6.36$ (continuous line) and $y_{wt} = 0.10t + 731.2$ (dotted line). The wave tip has accelerated in the x -direction compared to the data from the visualization camera (dashed-dotted line). The y_{wt} coordinate deviates from the linear fit of the visualization camera for $t > -5$ ms, which shows an acceleration of the wave tip coordinate in the y -direction.

on the free surface in front the wave tip.⁶⁸ In the y -direction, the wave tip trajectory is altered by the gas flow escaping from the gas pocket, which is obvious from the acceleration in the y -direction for $-5 \leq t \leq 0$ ms. The wave tip trajectory in the y -direction is not comparable to that of a plunging breaking, which typically shows a ballistic trajectory.³² The wave velocity at the center plane can increase due to the wave focusing of a concave wave crest^{4,11} or Bernoulli

suction,⁵⁷ where the air pressure drops due to an increase in velocity at the wave crest.

A small amplitude wave grows on the wave crest for every wave impact, which is either caused by the large gradient of the free surface profile or by the Bernoulli suction (i.e., which is equivalent to the growth of a Kelvin–Helmholtz instability).^{32,49,57} However, the growth of a Kelvin–Helmholtz instability is, in this study, not expected, as there are no small scale disturbances observed on both the reconstructed free surface profiles and the shadowgraphs of the original stereo-PLIF images. Nonetheless, the small amplitude wave is defined as the wave tip, that is, the maximum x -coordinate of the wave crest.

The wave tip is observed to grow as it approaches the wall, which results in a thinner and longer wave tip.³² The length change in the wave tip is linear, up to approximately $t = -5$ ms, with respect to the global wave tip velocity $\dot{x}_{wt} \sim 1.2\sqrt{gh_0}$. In this time, the tip stretches approximately $L \sim (1.5 - 1.2)\sqrt{gh_0}\Delta t \sim 15$ mm, which is, based on visual inspection, a good estimate of the tip length. The stretched wave tip resembles a liquid sheet.

Villermaux and Clanet⁵⁹ studied the breakup of a liquid sheet formed by the impact of a jet on a circular disk. The liquid sheet expands into the surrounding air, which results in a shear force that destabilizes the sheet by an initial Kelvin–Helmholtz instability. The waves that result from the Kelvin–Helmholtz instability induce an additional motion at the tip of the liquid sheet. This finite motion at the tip of the liquid sheet provides the acceleration required for a secondary Rayleigh–Taylor instability.

A similar type of mechanism is observed to trigger the development of a span-wise instability on the tip of a plunging breaking wave. The wave tip is stretched into a thin liquid sheet, which is destabilized by an initial Kelvin–Helmholtz instability. This is observed as a finite amplitude wave that forms on the wave tip for $t > -5$ ms [panels (a) and (b) of Fig. 12]. The finite amplitude wave,

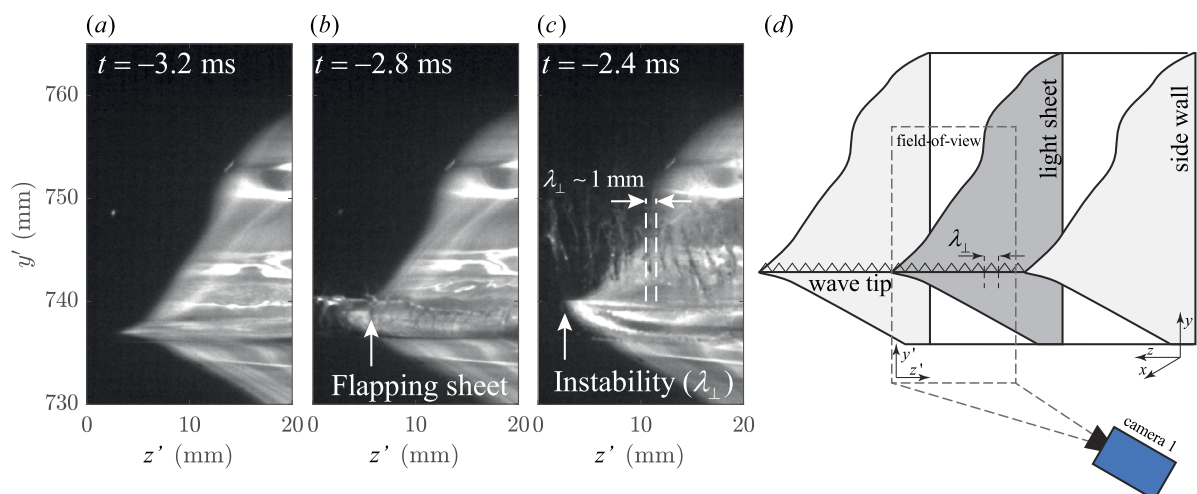


FIG. 12. The images of camera 1 are back-projected to a plane parallel to the impact wall [(a)–(c)]. (a) A typical wave (M221) approaches the wall and the tip elongates. (b) The elongated wave tip is destabilized by a shear instability. (c) A flapping liquid sheet develops with a spanwise wavelength (λ_{\perp}) defined by the Rayleigh–Taylor instability. (d) The images are acquired with camera 1 of the stereo-PLIF system (Fig. 1). The camera images the wave from the front at an angle with respect to the light sheet. Note the difference in coordinate system compared to that defined in Fig. 1.

combined with the acceleration of the wave tip by the gas flow, results in an acceleration that triggers a Rayleigh–Taylor instability [Fig. 12(c)]. The wavelength of the span-wise instability (i.e., liquid filaments or fingers) is defined as

$$\lambda_{\perp} \sim (\gamma/\rho_a \dot{x}_{wt}^2)(\rho_a/\rho_l)^{1/3}, \quad (4)$$

where $\dot{x}_{wt} = 1.5\sqrt{gh_0}$ is the wave tip velocity, γ is the surface tension of the air–water interface (72.3 mN m^{-1}), ρ_a is the gas density (1.23 kg m^{-3}), and ρ_l is the liquid density (998 kg m^{-3}) at standard atmospheric conditions (1 bar, 20°C). The spanwise wavelength of approximately $\lambda_{\perp} \sim 1 \text{ mm}$ agrees well with the visually observed finger spacing [Fig. 12(c)].

In previous work, the impact pressure variability was shown to depend on the density ratio (ρ_a/ρ_l) and the surface tension. A higher density ratio results in more well-developed (i.e., larger) liquid filaments.^{39,40} Furthermore, the free surface at the wave crest fragments earlier for lower values of the surface tension.³⁸ The increase in liquid filaments at higher density ratios and the spray formation at lower surface tension values are both captured by the span-wise wavelength of the Rayleigh–Taylor instability in Eq. (4). A mechanism for the development of instabilities is presented, where a flapping liquid sheet develops into liquid filaments.⁴⁵ Furthermore, the liquid filaments are accelerated by the gas flow from the gas pocket and eventually breakup in small droplets due to a capillary instability of the liquid filament.⁶⁹

The variability in wave impact pressure is linked to the variation in wave impact location. However, the formation of liquid filaments decreases the accuracy of the wave tip detection prior to impact (i.e., close to the wall). The variation in wave impact location is, therefore, determined just prior to the formation of a flapping liquid sheet. The impact location is determined over a small time interval ($\Delta t = 2 \text{ ms}$) to improve the reliability of the measured coordinate. Figure 13 displays the variation in vertical wave tip location for $-6.0 \leq t \leq -4.0 \text{ ms}$

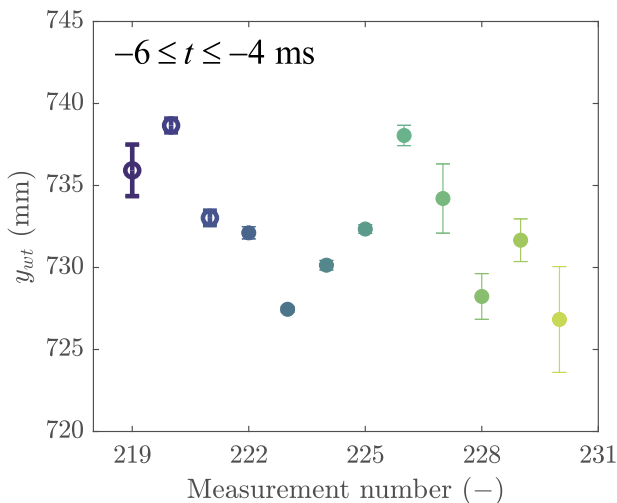


FIG. 13. The variation in vertical wave tip location (y_{wt}) for $-6.0 \leq t \leq -4.0 \text{ ms}$. The open markers are non-repeatable waves (i.e., outliers based on the surface elevation measurements) and closed markers are repeatable waves.

$\leq -4.0 \text{ ms}$, which is an indication of the variation in wave impact location.

The variation in vertical wave tip location is significant on a global scale with a standard deviation of 4 mm (i.e., 0.5% of the typical wave height). The membrane surface ($d \sim 1 \text{ mm}$ to 5.5 mm)^{19,58} of a typical pressure sensor is small compared to the variation in vertical wave tip location. Even for large ($d \sim 9.5 \text{ mm}$) pressure sensor membranes, the integrating effect of the surface area is not sufficient to remove all pressure variability.¹⁷ Furthermore, the physical spacing of the pressure sensor, which is typically on the order of 20 mm,^{19,37} limits the possibility of detecting these small wave tip variations. The variation in vertical wave tip location is similar to the other, not reported, measurements. However, the measurements cannot be combined due to the significant day-to-day variations.

Additionally, very close to the wall ($x/h_0 \lesssim 0.18$), the wave tip accelerates to about $1.5\sqrt{gh_0}$ compared to the global wave velocity of $1.2\sqrt{gh_0}$. The pressure sensor membrane is hit with either the wave tip velocity or the global wave velocity, which can result in a pressure difference of $\sim 25\%$. The variation in pressure is similar to previous reported values for nominal identical waves.^{18,37} The variation in wave tip velocity due to either wave focusing or Bernoulli suction is a source of variability in impact pressure.

The source of impact pressure variation is a combination of system and hydrodynamic variability, but even for well-repeated waves (i.e., with insignificant system variability), a significant wave tip variability is observed. The variability in vertical wave tip location over repeated waves on a single day is shown to be significant compared to typical pressure membrane diameters (i.e., $d_p \approx 1 \text{ mm}$ – 5.5 mm). Furthermore, this variation is observed over several other days with a similar order of magnitude. The hydrodynamic variability is, even when the waves are well repeated, a source of pressure variability. The shear-driven flapping motion of the liquid sheet results in significant variability in the impact location, which also triggers a Rayleigh–Taylor type of instability along the spanwise direction of the wave. The presented mechanism is probably one of the many types of instabilities that can occur on the wave crest, but for the reported gas pocket impact, it occurs over a significant range of wave shapes. The reported measurements can be used for physical and numerical model validation.

IV. CONCLUSION

Repeated focused wave impacts on a vertical wall are reported. The generation of repeatable focused waves is not trivial. A limited number (i.e., $N = 12$) of the total set of 32 measurements is reported, as the day-to-day variations limit the detailed comparison. Therefore, the experimental variability (i.e., system variability) is reported in detail, which indicates that the wave generation is well-repeated over a single day. Several repeatable waves are identified ($N = 9$) based on the surface-elevation measurements. These repeatable waves are studied and compared to the remaining non-repeatable waves ($N = 3$).

The global wave behavior prior to impact is studied with a visualization camera. The cross-sectional area of a large gas pocket impact is approximated by a semiellipse constrained to the impact wall. The aspect ratio of the ellipse is relatively constant $R_x/R_y = 1.6 (\sim \sqrt{3})$, which is comparable to that of a plunging breaker.³³

Initially, the global wave behavior is also comparable to that of a plunging breaker, as both have a similar wave velocity ($\sqrt{gh_0}$) and wave tip velocity ($1.2\sqrt{gh_0}$). However, the trajectory of the wave tip does not resemble that of a plunging breaker. The drag at the wave crest, due to the escaping gas velocity, partially counteracts the gravitational force. Furthermore, the wave tip accelerates to a velocity of $1.5\sqrt{gh_0}$ as it approaches the wall ($x/h_0 \lesssim 0.18$).

Moments before impact, the wave tip is deflected by the strong gas flow at the wave crest. The wave tip resembles a liquid sheet that is destabilized by an initial Kelvin–Helmholtz instability. A flapping liquid sheet develops, and the acceleration of the tip triggers a Rayleigh–Taylor instability. The spanwise wavelength of the Rayleigh–Taylor instability is well approximated by $\lambda_{\perp} \sim (\gamma/\rho_a \dot{x}_{wt}^2)(\rho_a/\rho_l)^{1/3}$. The Rayleigh–Taylor instability is one of the free surface instabilities that can be a source of wave impact pressure variability. Furthermore, the flapping liquid sheet is an indication of an instability that results in pressure variability with varying density ratio (ρ_a/ρ_l) and surface tension (γ). The other, not reported, measurements show a similar wave crest development with a flapping liquid sheet that triggers a Rayleigh–Taylor instability.

In previous work, the variability in impact pressure is often attributed to Kelvin–Helmholtz type instabilities at the wave crest.⁴ The current work shows that the variability in impact location is initially drag induced, with a standard deviation in impact location of $\sim 0.5\%$ compared to a wave height of 732.4 mm. The variation in impact location is large compared to typical contemporary pressure sensor sizes. A shear-driven flapping liquid sheet develops moments before impact, which delays the impact time and triggers a Rayleigh–Taylor instability that forms equally spaced liquid filaments. However, the variability in impact height already exists before the formation of the liquid filaments. The liquid filaments can impact the pressure sensor, although it is more likely that the wave tip will directly impact the pressure sensor. The acceleration of the wave tip compared to the wave crest and global wave presents a more likely explanation of the variance in impact pressure.

SUPPLEMENTARY MATERIAL

See the [supplementary material](#) for a movie of a typical (i.e., M225) wave impact and the detailed structure of the wave tip for the 12 reported measurements.

ACKNOWLEDGMENTS

This work was part of the public–private research program Sloshing of Liquefied Natural Gas (SLING) (Project No. P14-10). The support by the Netherlands Organization for Scientific Research (NWO) Domain Applied and Engineering Sciences and project partners is gratefully acknowledged. The authors are grateful to the lab technicians at the Environmental Fluid Mechanics Laboratory of the Delft University of Technology for their assistance with the experimental setup and their support during the experiments.

DATA AVAILABILITY

The data that support the findings of this study are available from the corresponding author upon reasonable request.

REFERENCES

- R. Aronietis, C. Sys, E. van Hassel, and T. Vanelander, “Forecasting port-level demand for LNG as a ship fuel: The case of the port of Antwerp,” *J. Ship Trade* **1**, 2 (2016).
- L. Delorme, A. Colagrossi, A. Souto-Iglesias, R. Zamora-Rodríguez, and E. Botía-Vera, “A set of canonical problems in sloshing, Part I: Pressure field in forced roll—Comparison between experimental results and SPH,” *Ocean Eng.* **36**, 168–178 (2009).
- B. Buchner and T. Bunnik, “Extreme wave effects on deepwater floating structures,” in Offshore Technology Conference, 2007.
- D. H. Peregrine, “Water-wave impact on walls,” *Annu. Rev. Fluid Mech.* **35**, 23–43 (2003).
- M. Ancellin, L. Brosset, and J.-M. Ghidaglia, “Numerical simulation of wave impacts with interfacial phase change: An isothermal averaged model,” *Eur. J. Mech.: B/Fluids* **72**, 631–644 (2018).
- R. A. Bagnold, “Interim report on wave-pressure research. (Includes plates and photographs),” *J. Inst. Civ. Eng.* **12**, 202–226 (1939).
- M. Hattori, A. Arami, and T. Yui, “Wave impact pressure on vertical walls under breaking waves of various types,” *Coast. Eng.* **22**, 79–114 (1994).
- P. A. Blackmore and P. J. Hewson, “Experiments on full-scale wave impact pressures,” *Coastal Eng.* **8**, 331–346 (1984).
- G. N. Bullock, A. R. Crawford, P. J. Hewson, M. J. A. Walkden, and P. A. D. Bird, “The influence of air and scale on wave impact pressures,” *Coastal Eng.* **42**, 291–312 (2001).
- G. Cuomo, W. Allsop, T. Bruce, and J. Pearson, “Breaking wave loads at vertical seawalls and breakwaters,” *Coastal Eng.* **57**, 424–439 (2010).
- A. Wang, C. M. Ikeda-Gilbert, J. H. Duncan, D. P. Lathrop, M. J. Cooker, and A. M. Fullerton, “The impact of a deep-water plunging breaker on a wall with its bottom edge close to the mean water surface,” *J. Fluid Mech.* **843**, 680–721 (2018).
- B. Hofland, M. Kaminski, and G. Wolters, “Large scale wave impacts on a vertical wall,” *Coastal Eng. Proc.* **1**(32), 15 (2010).
- O. Kimmoun, A. Ratouis, and L. Brosset, “Sloshing and scaling: Experimental study in a wave canal at two different scales,” in 20th International Ocean and Polar Engineering Conference, 20–25 June, Beijing, China, 2010.
- M. J. Cooker and D. H. Peregrine, “Pressure-impulse theory for liquid impact problems,” *J. Fluid Mech.* **297**, 193–214 (1995).
- E. de Almeida and B. Hofland, “Validation of pressure-impulse theory for standing wave impact loading on vertical hydraulic structures with short overhangs,” *Coastal Eng.* **159**, 103702 (2020).
- A. Ghadirian and H. Bredmose, “Pressure impulse theory for a slamming wave on a vertical circular cylinder,” *J. Fluid Mech.* **867**, R1 (2019).
- Y. K. Song, K.-A. Chang, Y. Ryu, and S. H. Kwon, “Experimental study on flow kinematics and impact pressure in liquid sloshing,” *Exp. Fluids* **54**, 1592 (2013).
- H. Bogaert, S. Léonard, L. Brosset, and M. L. Kaminsk, “Sloshing and scaling: Results from the sloshel project,” in 20th International Ocean and Polar Engineering Conference, 20–25 June, Beijing, China, 2010.
- W. Lafeber, H. Bogaert, and L. Brosset, “Comparison of wave impact tests at large and full scale: Results from the sloshel project,” in 22nd International Ocean and Polar Engineering Conference, 17–22 June, Rhodes, Greece, 2012.
- W. Lafeber, H. Bogaert, and L. Brosset, “Elementary loading processes (ELP) involved in breaking wave impacts: Findings from the sloshel project,” in 22nd International Ocean and Polar Engineering Conference, 17–22 June, Rhodes, Greece, 2012.
- Z.-J. Wei, O. M. Faltinsen, C. Lugni, and Q.-J. Yue, “Sloshing-induced slamming in screen-equipped rectangular tanks in shallow-water conditions,” *Phys. Fluids* **27**, 032104 (2015).
- Y. Wei, T. Abadie, A. Henry, and F. Dias, “Wave interaction with an oscillating wave surge converter. Part II: Slamming,” *Ocean Eng.* **113**, 319–334 (2016).
- A. Henry, T. Abadie, J. Nicholson, A. McKinley, O. Kimmoun, and F. Dias, “The vertical distribution and evolution of slam pressure on an oscillating wave surge converter,” in International Conference on Offshore Mechanics and Arctic Engineering, 2015.
- E. Renzi, Y. Wei, and F. Dias, “The pressure impulse of wave slamming on an oscillating wave energy converter,” *J. Fluids Struct.* **82**, 258–271 (2018).

- ²⁵R. A. Ibrahim, "Assessment of breaking waves and liquid sloshing impact," *Nonlinear Dyn.* **100**, 1837–1925 (2020).
- ²⁶F. Dias and J.-M. Ghidaglia, "Slamming: Recent progress in the evaluation of impact pressures," *Annu. Rev. Fluid Mech.* **50**, 243–273 (2018).
- ²⁷E. S. Chan and W. K. Melville, "Deep-water plunging wave pressures on a vertical plane wall," *Proc. R. Soc. London, Ser. A* **417**, 95–131 (1988).
- ²⁸C. Lugni, M. Brocchini, and O. M. Faltinsen, "Wave impact loads: The role of the flip-through," *Phys. Fluids* **18**, 122101 (2006).
- ²⁹C. Lugni, A. Bardazzi, O. M. Faltinsen, and G. Graziani, "Hydroelastic slamming response in the evolution of a flip-through event during shallow-liquid sloshing," *Phys. Fluids* **26**, 032108 (2014).
- ³⁰A. A. Korobkin, T. I. Khabakhpasheva, and S. Malenica, "Maximum stress of stiff elastic plate in uniform flow and due to jet impact," *Phys. Fluids* **29**, 072105 (2017).
- ³¹T. Vinje and P. Brevig, "Numerical simulation of breaking waves," *Adv. Water Resour.* **4**, 77–82 (1981).
- ³²M. Longuet-Higgins, "On the disintegration of the jet in a plunging breaker," *J. Phys. Oceanogr.* **25**, 2458–2462 (1995).
- ³³A. L. New, "A class of elliptical free-surface flows," *J. Fluid Mech.* **130**, 219–239 (1983).
- ³⁴P. Bonmarin, "Geometric properties of deep-water breaking waves," *J. Fluid Mech.* **209**, 405–433 (1989).
- ³⁵B. C. Abrahamsen and O. M. Faltinsen, "The effect of air leakage and heat exchange on the decay of entrapped air pocket slamming oscillations," *Phys. Fluids* **23**, 102107 (2011).
- ³⁶C. Lugni, M. Miozzi, M. Brocchini, and O. M. Faltinsen, "Evolution of the air cavity during a depressurized wave impact. I. The kinematic flow field," *Phys. Fluids* **22**, 056101 (2010).
- ³⁷C. Lugni, M. Brocchini, and O. M. Faltinsen, "Evolution of the air cavity during a depressurized wave impact. II. The dynamic field," *Phys. Fluids* **22**, 056102 (2010).
- ³⁸M. Frihat, L. Brosset, and J. M. Ghidaglia, "Experimental study of surface tension effects on sloshing impact loads," in Proceedings of International Workshop on Water Waves and Floating Bodies, 23–26 April, Dalian, China, 2017.
- ³⁹M. R. Karimi, L. Brosset, J.-M. Ghidaglia, and M. L. Kaminski, "Effect of ullage gas on sloshing, Part I: Global effects of gas-liquid density ratio," *Eur. J. Mech.: B/Fluids* **53**, 213–228 (2015).
- ⁴⁰M. R. Karimi, L. Brosset, J.-M. Ghidaglia, and M. L. Kaminski, "Effect of ullage gas on sloshing, Part II: Local effects of gas-liquid density ratio," *Eur. J. Mech.: B/Fluids* **57**, 82–100 (2016).
- ⁴¹M. Ancellin, L. Brosset, and J.-M. Ghidaglia, "Numerical simulation of wave impacts with interfacial phase change: An interface reconstruction scheme," *Eur. J. Mech.: B/Fluids* **76**, 352–364 (2019).
- ⁴²M. Ancellin, L. Brosset, and J.-M. Ghidaglia, "Numerical study of phase change influence on wave impact loads in LNG tanks on floating structures," in International Conference on Offshore Mechanics and Arctic Engineering, 2018.
- ⁴³H. Bredmose, G. N. Bullock, and A. J. Hogg, "Violent breaking wave impacts. Part 3. Effects of scale and aeration," *J. Fluid Mech.* **765**, 82–113 (2015).
- ⁴⁴G. N. Bullock, C. Obhrai, D. H. Peregrine, and H. Bredmose, "Violent breaking wave impacts. Part 1: Results from large-scale regular wave tests on vertical and sloping walls," *Coastal Eng.* **54**, 602–617 (2007).
- ⁴⁵P. Lubin, O. Kimmoun, F. Véron, and S. Glockner, "Discussion on instabilities in breaking waves: Vortices, air-entrainment and droplet generation," *Eur. J. Mech.: B/Fluids* **73**, 144–156 (2019).
- ⁴⁶S. Zhang, D. K. P. Yue, and K. Tanizawa, "Simulation of plunging wave impact on a vertical wall," *J. Fluid Mech.* **327**, 221–254 (1996).
- ⁴⁷B. Song and C. Zhang, "Water column impact on a rigid wall with air cavity effects," *Phys. Fluids* **31**, 042112 (2019).
- ⁴⁸B. Song and C. Zhang, "Boundary element study of wave impact on a vertical wall with air entrapment," *Eng. Anal. Boundary Elem.* **90**, 26–38 (2018).
- ⁴⁹S. Ross and P. D. Hicks, "A comparison of pre-impact gas cushioning and Wagner theory for liquid-solid impacts," *Phys. Fluids* **31**, 042101 (2019).
- ⁵⁰S. Etienne, Y.-M. Scolan, and L. Brosset, "Numerical study of density ratio influence on global wave shapes before impact," in International Conference on Offshore Mechanics and Arctic Engineering, 2018.
- ⁵¹P. M. Guilcher, Y. Jus, N. Couty, L. Brosset, Y.-M. Scolan, and D. Le Touzé, "2D simulations of breaking wave impacts on a flat rigid wall—Part 1: Influence of the wave shape," in 24th International Ocean and Polar Engineering Conference, 15–20 June, Busan, Korea (International Society of Offshore and Polar Engineers, 2014).
- ⁵²P. M. Guilcher, Y. Jus, and L. Brosset, "2D simulations of breaking wave impacts on a flat rigid wall—Part 2: Influence of scale," in 28th International Ocean and Polar Engineering Conference, 10–15 June, Sapporo, Japan, 2018.
- ⁵³S. Fortin, S. Etienne, C. Béguin, D. Pelletier, L. Brosset *et al.*, "Numerical study of the influence of Weber and Reynolds numbers on the development of Kelvin-Helmholtz instability," *Int. J. Offshore Polar Eng.* **30**, 129–140 (2020).
- ⁵⁴M. Frihat, M. R. Karimi, L. Brosset, J.-M. Ghidaglia *et al.*, "Variability of impact pressures induced by sloshing investigated through the concept of "singularization," in 26th International Ocean and Polar Engineering Conference, 26 June–2 July, Rhodes, Greece, 2016.
- ⁵⁵R. Firoozkoobi, B. C. Abrahamsen, and O. M. Faltinsen, "Study of an entrapped air pocket due to sloshing using experiments and numerical simulations," in International Conference on Offshore Mechanics and Arctic Engineering, 2017.
- ⁵⁶P. D. Hicks, "LNG-solid impacts with gas cushioning and phase change," *J. Fluids Struct.* **80**, 22–36 (2018).
- ⁵⁷I. R. Peters, D. van der Meer, and J. M. Gordillo, "Splash wave and crown breakup after disc impact on a liquid surface," *J. Fluid Mech.* **724**, 553–580 (2013).
- ⁵⁸A. Souto-Iglesias, G. Bulian, and E. Botia-Vera, "A set of canonical problems in sloshing. Part 2: Influence of tank width on impact pressure statistics in regular forced angular motion," *Ocean Eng.* **105**, 136–159 (2015).
- ⁵⁹E. Villermaux and C. Clanet, "Life of a flapping liquid sheet," *J. Fluid Mech.* **462**, 341–363 (2002).
- ⁶⁰M. van Meerkerk, C. Poelma, and J. Westerweel, "Scanning stereo-PLIF method for free surface measurements in large 3D domains," *Exp. Fluids* **61**, 19 (2020).
- ⁶¹J. H. Duncan, H. Qiao, V. Philomin, and A. Wenz, "Gentle spilling breakers: Crest profile evolution," *J. Fluid Mech.* **379**, 191–222 (1999).
- ⁶²N. Otsu, "A threshold selection method from gray-level histograms," *IEEE Trans. Syst., Man, Cybern.* **9**, 62–66 (1979).
- ⁶³R. C. Gonzalez, R. E. Woods, and S. L. Eddins, *Digital Image Processing Using Matlab* (Gatesmark Publishing, 2009).
- ⁶⁴R. J. Adrian and J. Westerweel, *Particle Image Velocimetry* (Cambridge University Press, 2011), Vol. 30.
- ⁶⁵V. Pratt, "Direct least-squares fitting of algebraic surfaces," *ACM SIGGRAPH Comput. Graphics* **21**, 145–152 (1987).
- ⁶⁶J. H. Friedman, J. L. Bentley, and R. A. Finkel, "An algorithm for finding best matches in logarithmic expected time," *ACM Trans. Math. Software* **3**, 209–226 (1977).
- ⁶⁷V. Novaković, J. J. Costas, S. Schreier, O. Kimmoun, A. Fernandes, R. Ezeta, M. Birvalski, and H. Bogaert, "Study of global wave repeatability in the new Multiphase Wave Lab (MWL)," in 30th International Ocean and Polar Engineering Conference, 12–16 October, Shanghai, China, 2020.
- ⁶⁸G. Chen, C. Kharif, S. Zaleski, and J. Li, "Two-dimensional Navier–Stokes simulation of breaking waves," *Phys. Fluids* **11**, 121–133 (1999).
- ⁶⁹P. Marmottant and E. Villermaux, "On spray formation," *J. Fluid Mech.* **498**, 73–111 (2004).